ARTICLES
https://doi.org/10.1038/s41566-018-0224-2
nature photonics

Nano-optic endoscope for high-resolution optical coherence tomography in vivo

Hamid Pahlevaninezhad[1,2,6], Mohammadreza Khorasaninejad[2,6], Yao-Wei Huang[2,3,6], Zhujun Shi[4], Lida P. Hariri[1], David C. Adams[1], Vivien Ding[2,5], Alexander Zhu[2], Cheng-Wei Qiu[3], Federico Capasso[2]* and Melissa J. Suter[1]*

Acquisition of high-resolution images from within internal organs using endoscopic optical imaging has numerous clinical applications. However, difficulties associated with optical aberrations and the trade-off between transverse resolution and depth of focus significantly limit the scope of applications. Here, we integrate a metalens, with the ability to modify the phase of incident light at subwavelength level, into the design of an endoscopic optical coherence tomography catheter (termed nano-optic endoscope) to achieve near diffraction-limited imaging through negating non-chromatic aberrations. Remarkably, the tailored chromatic dispersion of the metalens in the context of spectral interferometry is utilized to maintain high-resolution imaging beyond the input field Rayleigh range, easing the trade-off between transverse resolution and depth of focus. We demonstrate endoscopic imaging in resected human lung specimens and in sheep airways in vivo. The combination of the superior resolution and higher imaging depth of focus of the nano-optic endoscope is likely to increase the clinical utility of endoscopic optical imaging.

Endoscopic optical imaging using fibre optic catheters has provided numerous opportunities for obtaining information from remote, hard-to-reach places with several applications including medical imaging. In particular, endoscopic optical coherence tomography (OCT)[1,2], capable of providing detailed images of tissue microstructure millimetres deep into the tissue, is emerging as a promising tool for detection, diagnosis and monitoring of disease in luminal organs such as the coronary arteries[3–5], the gastrointestinal tract[6,7] and the pulmonary airways[8,9]. However, despite pressing clinical needs for tools and instruments capable of accurately visualizing pathology including the extension of lesions in luminal organs, volumetric endoscopic optical imaging techniques have not been translated into routine clinical practice in many applications. A possible reason for this, among others, is the shortcomings associated with each technique. Some imaging modalities such as confocal endomicroscopy provide sufficient resolution to visualize tissue structures even at the cellular level but lack adequate penetration depth and field of view necessary for impact in many clinical applications. Others such as conventional OCT provide increased depth range and field of view but fall short of desired resolution. Difficulties associated with optical aberrations and the trade-off between the transverse resolution and the depth of focus continue to plague clinical adoption.

OCT was originally developed based on low-coherence interferometry[10,11] to acquire images of optical scattering from sub-surface tissue structures by measuring the cross-correlation function[12,13]. Demands for high-speed acquisition crucial to wide-field imaging of luminal organs led to the advent of Fourier-domain techniques[14–18] that measure the spectral density function to obtain a depth-resolved line profile of tissue through Fourier transformation with significantly improved sensitivity. In practice, the spectral density function is measured using either a broadband light source–interferometer–spectrometer configuration or a wavelength-swept light source–interferometer–fast detector configuration.

Increasing the resolution of OCT systems has recently been the subject of intense research[19–26]. This is typically achieved by using light sources with shorter wavelengths with broader bandwidths to improve axial and lateral resolution. However, apart from technical difficulties associated with these systems, a fundamental limitation is the greatly increased scattering at shorter wavelengths that severely limits light penetration and, in turn, imaging depth in tissue[20,21].

Another important concern is that imaging with high lateral resolution by tightly focusing the illumination light greatly reduces the depth of focus, leading to the maintenance of high lateral resolution imaging for only a very short depth range. Different approaches have been proposed for the extension of depth of focus in the endoscopic settings, including illumination with multiple beams of different focal lengths using a combination of multiple fibres and a complex arrangement of miniature optical lenses[27] and addition of annular amplitude and/or phase filters to generate axially elongated illumination beams[23,24]. These techniques, however, result in reduced sensitivity and a compromise in lateral resolution due to the presence of side lobes. In addition, diffraction-limited imaging cannot be reached with these techniques due to spherical aberration and astigmatism (resulting from azimuthal symmetry of the focusing elements and the filters together with asymmetric curvatures of the protective layers in the optical path).

Apart from the aforementioned modifications and others[28,29], OCT catheters typically utilize the same basic principle. The optical field delivered through a length of single-mode fibre to the distal

[1]Department of Medicine, Pulmonary and Critical Care Division, Massachusetts General Hospital and Harvard Medical School, Boston, MA, USA. [2]Harvard John A. Paulson School of Engineering and Applied Sciences, Harvard University, Cambridge, MA, USA. [3]Department of Electrical and Computer Engineering, National University of Singapore, Singapore, Singapore. [4]Department of Physics, Harvard University, Cambridge, MA, USA. [5]University of Waterloo, Waterloo, Ontario, Canada. [6]These authors contributed equally to this work: Hamid Pahlevaninezhad, Mohammadreza Khorasaninejad, Yao-Wei Huang. *e-mail: capasso@seas.harvard.edu; msuter@mgh.harvard.edu

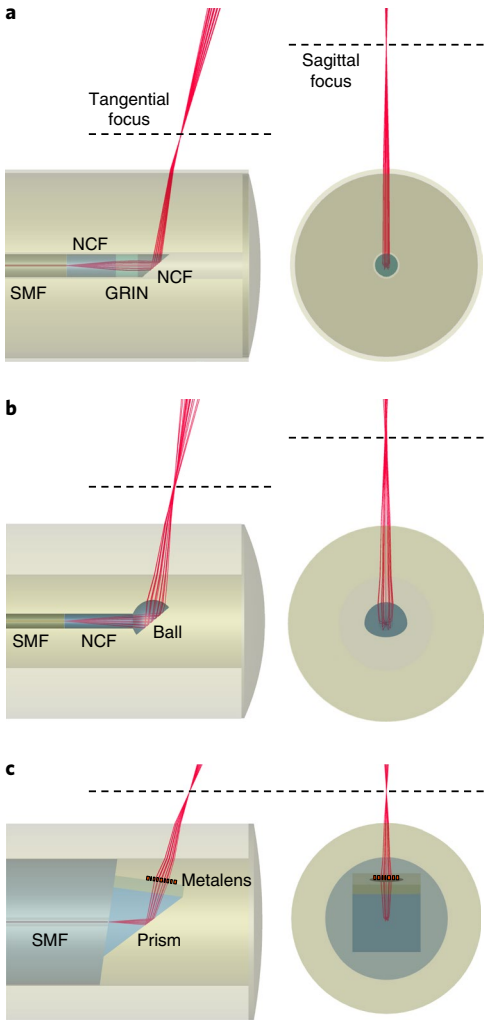

Fig. 1 | Endoscopic OCT catheter designs. a,**b**, Schematics of standard graded-index (GRIN) lens (**a**) and ball lens (**b**) OCT catheters. The output beams of these catheters suffer from aberrations including astigmatism primarily due to the presence of the cylindrical outer protective sheath with asymmetric curvatures in the transverse plane. **c**, Schematic of the nano-optic endoscope that uses a metalens to achieve near diffraction-limited focusing. NCF, no-core fibre; SMF, single-mode fibre.

end of the catheter is redirected and focused into the tissue using either a graded-index (GRIN) lens–prism configuration[1] (Fig. 1a) or an angle-polished ball lens[30] (Fig. 1b). This optical assembly is encased in a stationary transparent protective sheath. Images are captured by helically scanning the optical beam within the tissue lumen using distal or proximal actuators. Although the simplicity of the basic design has allowed these catheters to be utilized in numerous clinical applications, there are several shortcomings. Constraints in the shape of ball lenses (fabrication of a miniature lens with arbitrary shape is difficult) and the index profile of GRIN lenses (typical manufacturing techniques[31] only allow azimuthally symmetric near quadratic index profile with small refractive index contrasts) result in spherical aberrations and thus deviation from diffraction-limited focusing. In addition, the presence of multilayered structures in the optical path from the fibre facet to the focal point degrades the focusing quality. For example, the protective sheath introduces significant astigmatism owing to the different curvatures parallel and perpendicular to the catheter axis. Furthermore, optical properties of the output beam such as chromatic dispersion and polarization states cannot be modified. These significant limitations cannot be rectified in the current OCT catheter designs as the shape and refractive index profile of the focusing elements are not readily adjustable.

Here, we introduce a new class of fibre optic catheters using metalenses[32,33] that consist of arrays of subwavelength-spaced scatterers at an interface. Based on their geometric parameters and distribution, these optical scatterers locally shift the phase of the incident light and shape its wavefront, enabling realization of a wide variety of planar optical devices such as metalenses[34] and holograms[35,36]. The ability to tailor the phase at will with high spatial resolution allows metalenses to be free of spherical aberration and astigmatism, overcoming the essential barriers to diffraction-limited focusing and imaging. Notably, this technique can be used to achieve high-quality focusing in any complex medium with arbitrary refractive index profile and geometry. We integrate a metalens into the design of an endoscopic OCT catheter (termed nano-optic endoscope, Fig. 1c) and demonstrate high-resolution imaging at extended depth of focus with no requirements for additional acquisition and/or processing time[37] or complex arrangements of optical elements[27]. Crucially, the tailored chromatic dispersion of the metalens in the context of spectral interferometry allows for the maintenance of high-resolution imaging significantly beyond the Rayleigh range of the incident light. We compare the nano-optic endoscope to a commercial GRIN lens catheter and a ball lens catheter to assess output beam quality and to highlight the superior performance of the former. The ability of the nano-optic endoscope to obtain high-resolution images of sub-surface tissue structures in vivo is likely to increase the clinical utility of OCT in detection, diagnosis and monitoring of diseases.

Design and fabrication

A schematic of the nano-optic endoscope is depicted in Fig. 2a. Light is delivered and subsequently collected through a length of single-mode fibre housed within a drive cable and a ferrule with an 8° angle-polished end facet to reduce reflections. A prism attached to the ferrule redirects the light towards the metalens, for a side-viewing catheter suitable for imaging luminal organs. The transmissive metalens comprised of amorphous silicon (a-Si) nanopillars on a 170-μm-thick cover glass focuses and collects light to and from a target object (for example tissue). Figure 2b shows a photographic image of the fabricated nano-optic endoscope. The optical components at the distal end of the catheter were assembled using a custom-built platform comprised of holders for the metalens, fibre, and prism mounted on separate translational and rotational stages to ensure accurate alignment. The components were bonded using optical adhesive during simultaneous monitoring of the output beam to ensure the optimal performance. A glass capsule surrounds the distal end of the optical core to prevent direct contact of the rotating probe with the tissue being imaged to protect the distal optics from contamination. The protective sheath is known to introduce aberrations including astigmatism owing to its different curvatures parallel and perpendicular to the endoscope axis. This is a common issue of standard OCT catheters.

We designed the metalens to focus light from the fibre facet (considered as a point source) located at (x_s, y_s, z_s) into a diffraction-limited spot at (x_f, y_f, z_f) free from spherical aberrations and astigmatism. To accomplish this, the metalens must impart the phase profile ϕ:

$$\phi = \frac{2\pi}{\lambda_0}(L_{chief} - L_{sl} - L_{lf}) \quad (1)$$

to null optical path length differences, where L_{sl}, L_{lf} and L_{chief} are point source-to-lens, lens-to-focal point, and chief ray (the shortest) optical path lengths, respectively, at the design wavelength $\lambda_0 = 1.31\,\mu m$ (Supplementary Section I). An analytic approach to calculating the required phase profile based on ray-tracing is

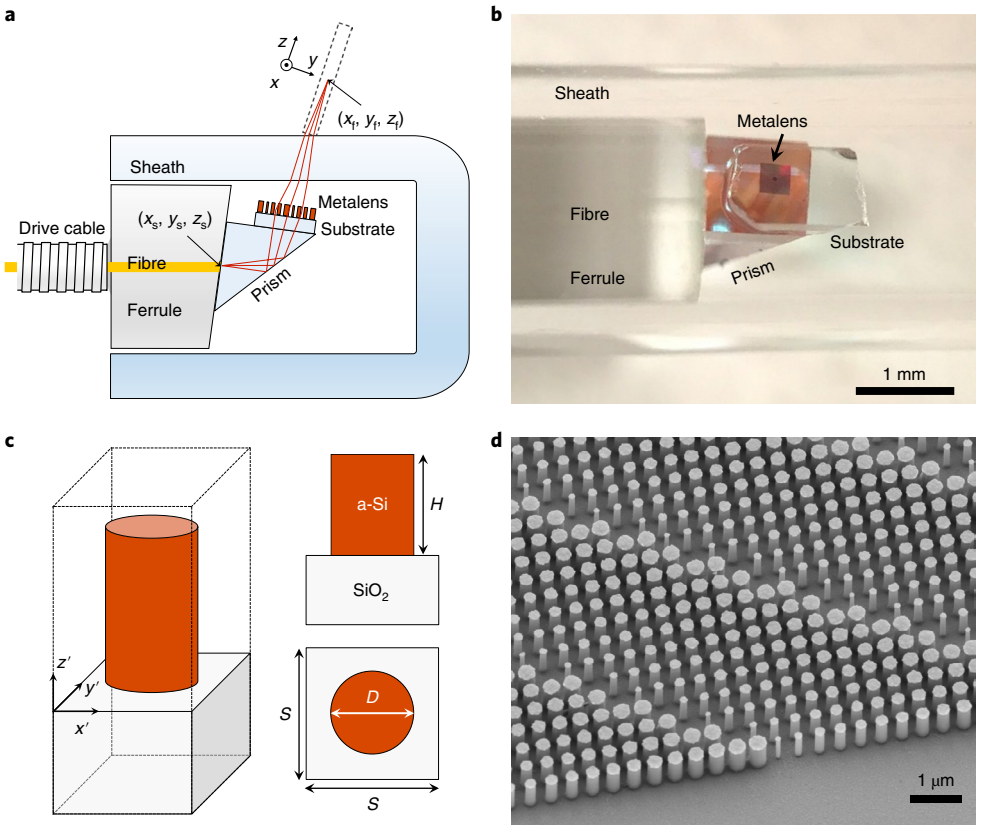

Fig. 2 | Nano-optic endoscope design and fabrication. a, Schematic of the nano-optic endoscope. The metalens was designed to image a point source at (x_s, y_s, z_s) to a diffraction-limited spot at (x_f, y_f, z_f) with working distance WD = 0.5 mm. **b**, Photographic image of the distal end of the nano-optic endoscope. **c**, Schematic of an individual metalens building block consisting of an amorphous silicon (a-Si) nanopillar on a glass substrate. The nanopillars have height $H = 750$ nm and are arranged in a square lattice with unit cell size $S = 400$ nm. Phase imparted by a nanopillar is controlled by its diameter (D). **d**, Scanning electron micrograph image of a portion of a fabricated metalens.

presented in the Supplementary Section I. The chromatic dispersion of the metalens is designed such that the focal point shifts only axially (along the propagation axis) with wavelength variations. Later we show that such chromatic dispersion enables maintaining high-resolution imaging in an extended depth range.

The metalens building blocks, a-Si nanopillars, have a height of 750 nm and varying diameters to locally impart the required phase. The azimuthal symmetry of a-Si nanopillars (Fig. 2c) results in a nearly polarization-independent metalens given the small range of incident angles (Supplementary Section II). This design is suitable for endoscopic optical imaging, where light exiting the single-mode fibre is randomly polarized due to the constant motion of the fibre during imaging. Owing to its high refractive index and low absorption in the near-infrared region, a-Si is an ideal material for the nanopillars in order to construct high-efficiency metalenses in this wavelength range. The high refractive index of a-Si allows closely packed nanopillars that fulfill the Nyquist sampling criterion ($S < \frac{\lambda}{2\mathrm{NA}}$, where NA is numerical aperture and S the unit cell size, Fig. 2c) with negligible near-field coupling. Nanopillars with power transmittance larger than 80% (Supplementary Section II) were selected in our design for high-efficiency performance (Supplementary Fig. 2). Figure 2d shows a scanning electron microscope image of a metalens fabricated using the conventional top-down approach[38,39] (see Methods).

Characterization

We characterized the nano-optic endoscope analytically and experimentally. The nano-optic endoscope output beam was modelled using a Fresnel–Kirchhoff integral analysis (Supplementary Section III) and validated with the intensity profile measurements of the output beam. The imaging performance was subsequently assessed by modelling the OCT spectral interferometry using the nano-optic endoscope (Supplementary Section V) and measuring the imaging resolution and depth of focus using a resolution target. Detailed analytic models are presented in the Supplementary Information and measurements are described below.

We measured the three-dimensional intensity profile of the output beam at different wavelengths spanning from 1,250 nm to 1,370 nm (corresponding to the wavelength range of typical OCT light sources) using the set-up shown in Supplementary Fig. 4. Figure 3a shows the nano-optic endoscope output beam profiles in the tangential plane (corresponding to the region specified with the dashed rectangle in Fig. 2a) that are almost identical to those in the sagittal plane (Supplementary Fig. 6a), indicating negligible astigmatism. As expected, the focal point shifted axially with changing wavelength. Measured focal spots of the nano-optic endoscope in the lateral plane (xy-plane) shown in Fig. 3b had nearly symmetric profiles with 12.7, 8.4 and 7.4 μm full-widths at half-maximum (FWHM) at 1,250, 1,310 and 1,370 nm wavelengths, respectively. Higher numerical apertures at longer wavelengths due to the focal point axial shift give rise to a reduced focal spot size, consistent with our calculations based on the Fresnel–Kirchhoff integral analysis (Supplementary Fig. 3). The measured spot sizes are close to the values predicted using the Fresnel–Kirchhoff integral analysis and the diffraction limit (Supplementary Fig. 7).

Figure 3c and Supplementary Fig. 5 compare the output beam profiles of a commercial GRIN lens catheter and a ball lens catheter

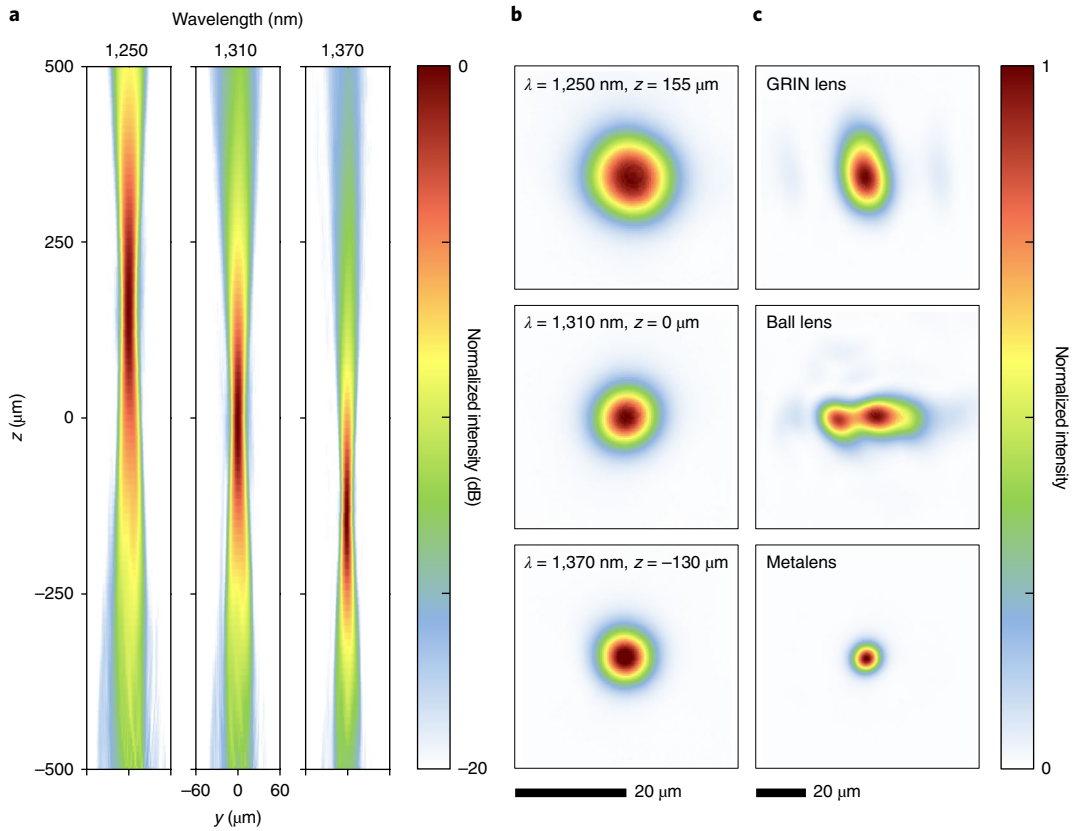

Fig. 3 | Optical characterization of the nano-optic endoscope and conventional OCT catheters. a, Measured intensity distribution of the output beam of the nano-optic endoscope along the propagation direction in the *yz*-plane (coordinates shown in Fig. 2a) at $\lambda = 1{,}250$, 1,310 and 1,370 nm. **b**, Focal spot profiles of the nano-optic endoscope at corresponding wavelengths. **c**, Focal spot profiles of a graded-index (GRIN) OCT catheter, a ball lens OCT catheter and the nano-optic endoscope at 1,310 nm wavelength. The incorporation of the metalens as the focusing element enables tighter focus with negligible astigmatism.

(see Methods) with those of the nano-optic endoscope. Significantly larger astigmatism, gauged as the distance between focal points in the tangential and sagittal planes, was measured for the GRIN lens (410 μm) and the ball lens (722 μm) catheters compared with that of the nano-optic endoscope (22 μm). As evident in Fig. 3c, the nano-optic endoscope focal spot profile was largely symmetric with appreciably smaller FWHM compared with the profiles of the GRIN lens (24 μm, 15 μm FWHMs in the focal plane) and the ball lens (11.6 μm, 35 μm FWHMs in the focal plane) catheters. It is difficult to determine the focal plane location for highly astigmatic optical beams; we chose the focal plane at the maximum intensity in our measurements. Ideally, the output beam profile of the nano-optic endoscope would be compared with that of conventional catheters of the same NA. However, the comparison is still valid given that the output beam profile of the higher NA nano-optic endoscope is of significantly higher quality despite the more noticeable effects of aberrations for higher NA lenses. Supplementary Figure 5 illustrates more detailed beam profiles of the three catheters.

OCT systems often use refractive lenses with low NAs to image samples with relatively long depth of focus. Chromatic dispersion of these lenses is typically insignificant. Therefore, the spectral interferometry analysis used for reconstruction of scattering amplitudes typically assumes a wavelength-independent incident beam[40,41]. When metalenses are used, this assumption is not valid since the chromatic dispersion normally follows that of diffractive optics and is therefore significant. Although there are techniques to reduce, increase, or reverse chromatic dispersion of metalenses to suit specific applications[42–44], the effects of chromatic dispersion of the metalens must be considered in the spectral interferometry analysis. We present an analytic approach to spectral interferometry with chromatic lenses detailed in Supplementary Section V. As summarized in Supplementary Fig. 8, this analysis predicts significantly larger imaging depth of focus for the nano-optic endoscope compared with the imaging depth of focus when an achromatic lens with the same NA is used. Spectral interferometry with the nano-optic endoscope uses backscattered signals from excitation beams at different wavelengths with varying focal points due to the metalens chromatic dispersion. This gives rise to imaging with effective axially shifted, overlapping field distributions with extended depth of focus that is larger than that produced by an achromatic lens (which is equivalent to a single wavelength excitation beam when determining the imaging depth of focus).

To experimentally measure the imaging resolution and depth of focus, we used a phantom comprised of a subwavelength gold line (width, 200 nm; height, 50 nm) on a glass substrate fabricated using electron-beam lithography (see Methods). The nano-optic endoscope was connected to a Fourier-domain OCT system[45,46] (details of which are provided in Supplementary Section VI), including a Mach–Zehnder interferometer driven by a swept source in the near-infrared wavelength range (1,240 to 1,350 nm). Resolution in the tangential and sagittal planes was obtained by scanning the target pattern across the nano-optic endoscope output beam using an automated translational stage with the endoscope axis perpendicular and parallel to the line, respectively. Measurements were repeated multiple times for reliable evaluation of the resolution at different depth points. Figure 4a shows the measured point spread

functions with smallest FWHMs of 6.37 μm (tangential) and 6.53 μm (sagittal). These values were slightly smaller than predictions likely due to small deviations from the linear response of the detector. The modulation transfer functions (MTF), the modulus of Fourier transform of the measured point spread functions, at different depth points are shown in Fig. 4b. Graphs of measured FWHMs and spatial frequency at 10% modulation contrast are shown in Fig. 4c. Solid lines and coloured regions represent polynomial fits to the repeated measurements and standard deviations, respectively. Comparison of the results in the tangential and sagittal planes indicates small astigmatism (22 μm) likely due to alignment imperfections during the endoscope assembly. The lateral resolution appears best at approximately 500 μm from the nano-optic endoscope outer surface (along the propagation direction), consistent with our analytic prediction. The effective depth of focus (the depth range in which FWHMs $<\sqrt{2}\mathrm{FWHM}_{\mathrm{min}}$) was 211 μm (tangential) and 315 μm (sagittal), significantly larger than that (90 μm) expected when an achromatic lens with the same NA is used (Supplementary Fig. 8b). The increased imaging depth-of-focus demonstrates yet another remarkable property of the nano-optic endoscope, namely flexible chromatic dispersion that can be utilized to achieve high-resolution imaging at extended depth of focus. Crucially, this outcome is not feasible to realize using refractive lenses.

Imaging

The nano-optic endoscope can be connected to standard OCT systems using a fibre optic rotary joint for endoscopic imaging. To demonstrate the imaging quality of the nano-optic endoscope in comparison with that of conventional OCT catheters, we performed imaging on fruit flesh (grape) and swine airways ex vivo. The fruit flesh exhibits fairly uniform cellular structures with small features (cellular walls) in the lateral and axial directions. Illustrated in Fig. 5b, the image captured using the nano-optic endoscope is notably of superior quality compared to that acquired using the ball lens catheter (Fig. 5a); cellular walls are more clearly visualized and small sized cells can be identified in the magnified images obtained using the nano-optic endoscope in contrast to those of the ball lens catheter. Figure 5c,d shows the comparison of the images obtained in the swine airway using a conventional ball lens catheter and the nano-optic endoscope. The clear delineation of the layers of the airway wall and the visualization of fine glands in the bronchial mucosa (arrow) further highlight the superior image quality of the nano-optic endoscope when compared with the corresponding images obtained with the conventional OCT catheter.

We tested the nano-optic endoscope in surgically resected human lung tissue specimens ex vivo and in the pulmonary airways of sheep in vivo.

The freshly excised lung tissue obtained from a patient with a lung nodule was inflated for imaging. OCT images of airways and alveolar structures were captured by inserting the nano-optic endoscope into the lungs both endobronchially and directly into the parenchyma. Figure 6a shows an image captured from a normal appearing airway. Features of the airway wall are clearly visible, including the epithelium, basement membrane and cartilage. Figure 6b shows a distal bronchiole through which multiple layers of small alveolar structures are visualized. In Fig. 6c, obtained from regions of abnormality on OCT, fine signal void structures are visible that correspond to irregular glands indicating the presence of adenocarcinoma[47]. Though the dimensions of these irregular glands approach the lateral resolution of conventional OCT catheters, they are clearly distinguishable with the nano-optic endoscope due to its superior resolution.

For preliminary evaluation of the nano-optic endoscope performance in vivo, we conducted a preclinical endobronchial OCT study in living sheep. The nano-optic endoscope was inserted through an endotracheal tube into the pulmonary airways. In vivo endobronchial imaging was performed at multiple sites in the tracheobronchial tree. An example image is provided in Fig. 6d, highlighting features in the airway wall microstructure including the epithelium, basement membrane, blood vessel and cartilage, and of the surrounding parenchyma where alveoli are clearly observed. Artefacts due to non-uniform rotational distortion were observed in a very small number of frames and only in instances when the endoscope was subjected to sharp and highly tortuous paths. Similar artefacts are commonly observed when using conventional OCT catheters in difficult-to-reach locations. This preclinical evaluation of the nano-optic endoscope indicated no significant flaws in the design for in vivo endoscopic imaging.

Discussion

Endoscopic OCT provides a wealth of information about the tissue sub-surface structures. However, the resolution and contrast of current endoscopic OCT catheters are not sufficient for several applications. For example, in lung nodules, although endoscopic OCT is able to readily detect squamous cell carcinoma due to the presence of large (>0.2 mm) nests of malignant cells[48], it can be challenging to accurately detect and diagnose adenocarcinoma where the characteristic atypical glandular features approach the resolution limit of such imaging systems. Improvements in the resolution and imaging depth of endoscopic OCT systems are crucial to increasing clinical utility. We speculate that the nano-optic endoscope will elevate the capabilities of endoscopic OCT in examining fine pathological changes in luminal tissue. Future clinically oriented studies may assess this hypothesis.

The outer diameter of the fabricated nano-optic endoscope presented in this work is 2.8 mm, larger than the sizes of OCT catheters typically used for endoscopic imaging of pulmonary airways and coronary arteries. The dimensions of the current nano-optic endoscope were chosen based on the availability of off-the-shelf components and for ease of endoscope assembly. However, there is no essential limitation to further miniaturization of the nano-optic endoscope, even to submillimeter diameters similar to other imaging catheters.

The versatility and design flexibility of the nano-optic endoscope enable new functionalities that are unattainable using conventional catheter fabrication techniques. One such example, as demonstrated in this work, is the ability to achieve high-resolution imaging through precise control of the phase of light to overcome spherical aberrations and astigmatism. High resolving power is among the most important advantages of optical imaging over other common medical imaging techniques such as sonography. Owing to its high-quality output beam and dispersion management, our nano-optic endoscope demonstrates high-resolution endoscopic imaging in vivo at extended depth of focus.

The ability to control other properties of output light such as the polarization state enables a host of other applications, implausible to achieve using conventional catheters. Several tissues, such as smooth muscle[49], collagen, either innate or in fibrosis[50], and blood vessels[51], have constituent structures highly organized in one particular direction. Polarization-sensitive imaging can differentiate these structures from surrounding tissue by detecting their innate birefringence and optic axis. However, determination of optic axis orientation is difficult in endoscopic imaging as the light exiting the catheter has an unknown polarization state due to fibre motion. Nano-optic endoscopes using polarization-sensitive metalenses can overcome these difficulties, enabling optical axis determination with no ambiguity. Further extension of imaging depth of focus using light sources with broader bandwidths and additional manipulation of metalens chromatic dis-

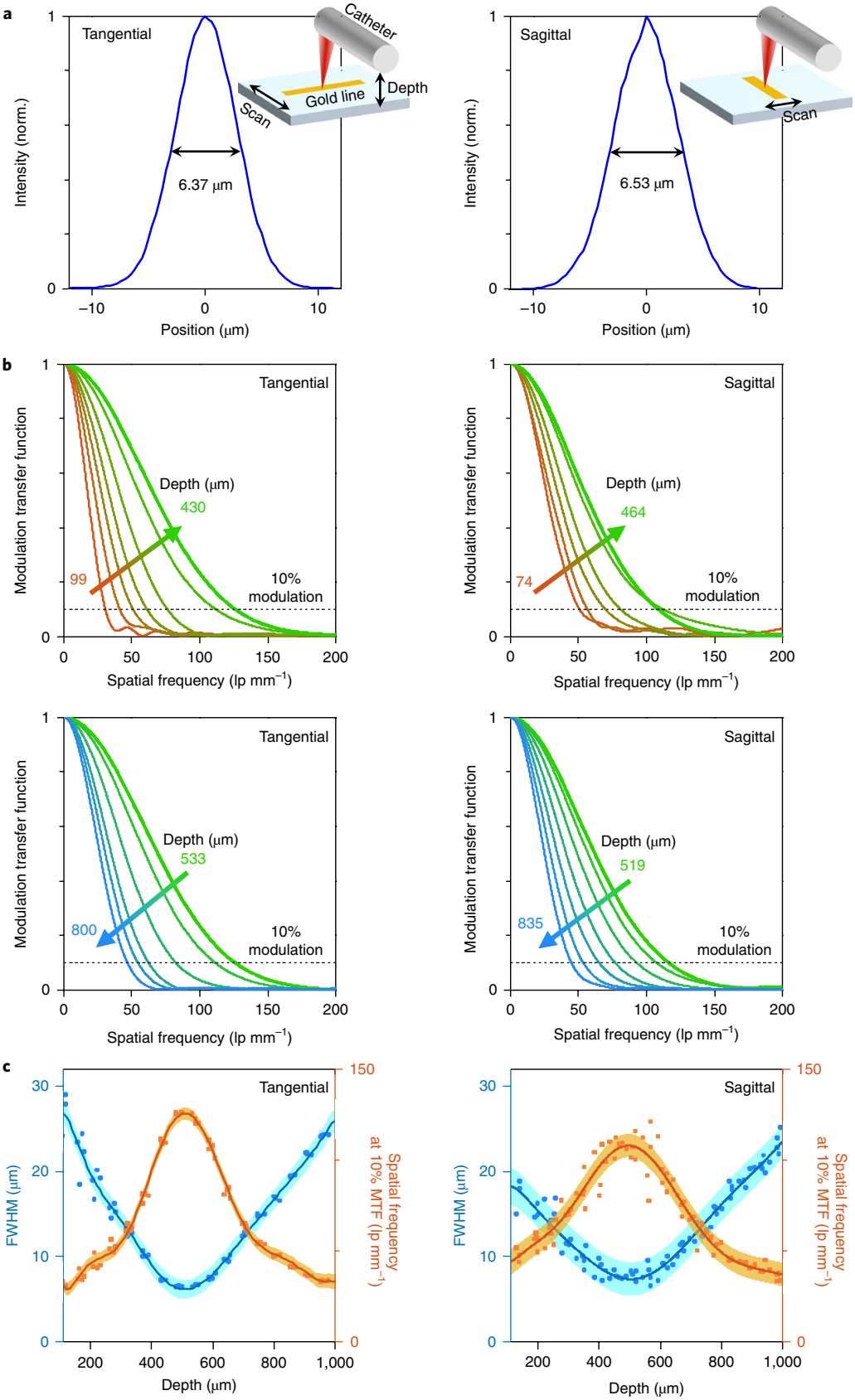

Fig. 4 | Resolution measurements of the nano-optic endoscope. a, Measured profiles of resolution target with the smallest full-widths at half maximum (FWHM) in the tangential and sagittal planes. **b**, Measured modulation transfer functions (MTF) at different depth points in the tangential and sagittal planes. **c**, FWHM and spatial frequency at 10% modulation contrast with respect to the depth in the tangential and sagittal planes. Coloured regions and solid lines indicate standard deviations and polynomial fits to the repeated ($n = 5$) measurements, respectively. lp, line pairs.

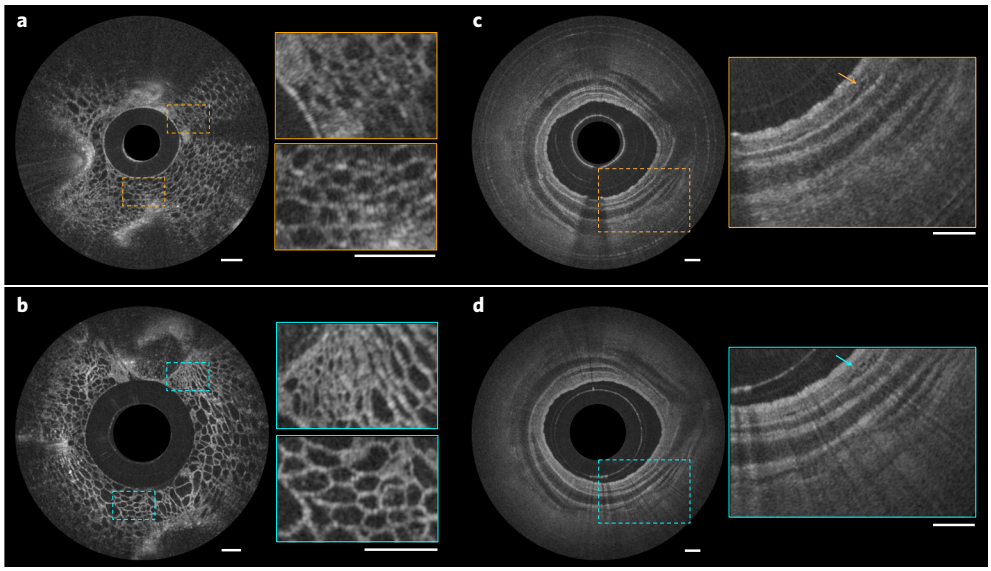

Fig. 5 | Comparison of OCT images acquired using the nano-optic endoscope and a conventional OCT catheter. a,**b**, OCT images of fruit flesh (grape) obtained using a ball lens catheter (**a**) and the nano-optic endoscope (**b**). **c**,**d**, Ex vivo images of swine airway using a ball lens catheter (**c**) and the nano-optic endoscope (**d**). The arrows indicate fine glands in bronchial mucosa. All scale bars, 500 μm.

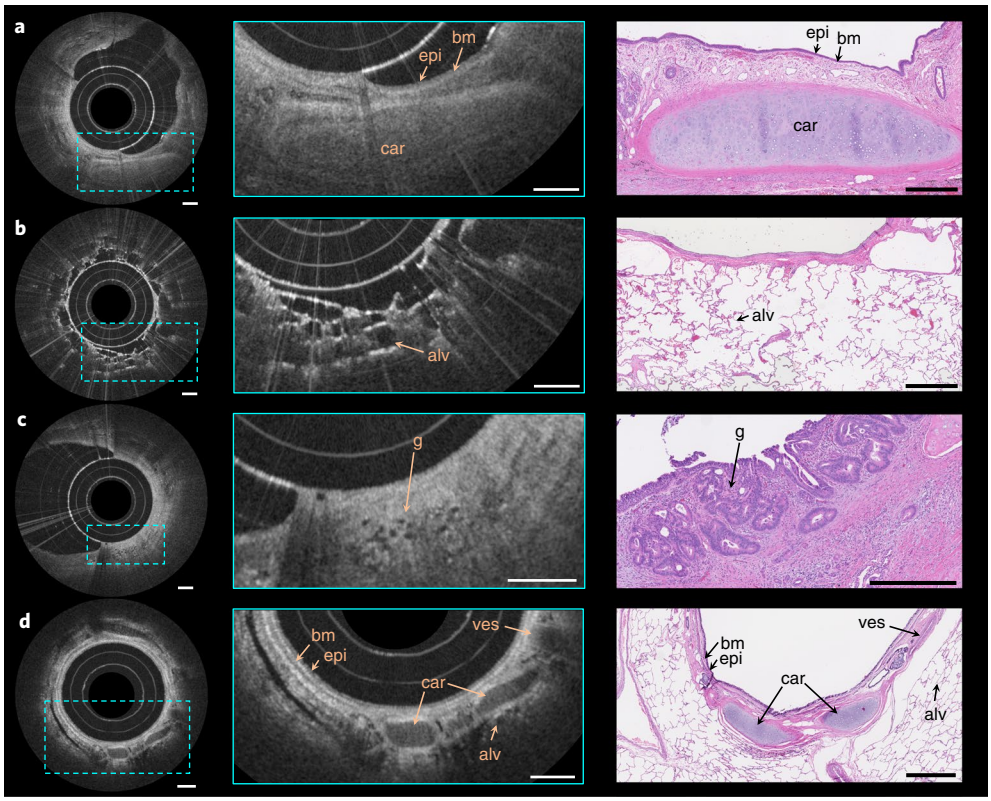

Fig. 6 | In vivo and ex vivo endoscopic OCT using the nano-optic endoscope. a–**d**, Endoscopic imaging of ex vivo human lung resections (**a**–**c**) and in vivo in the upper airways of sheep (**d**) using the nano-optic endoscope. Structural features of lung tissue are clearly visible in the magnified OCT images (centre column), including moderately scattering epithelium (epi), highly scattering basement membrane (bm), cartilage (car), blood vessel (ves) and alveoli (alv). Fine features, including the small irregular glands (g), the hallmark of adenocarcinoma, can be discerned. Representative histological images are provided in the right column. All scale bars, 500 μm.

persion is another important example. The unique properties of nano-optic endoscopes may also benefit other endoscopic optical imaging modalities such as confocal endomicroscopy for improved capabilities.

Methods

Methods, including statements of data availability and any associated accession codes and references, are available at https://doi.org/10.1038/s41566-018-0224-2.

Received: 19 December 2017; Accepted: 4 July 2018;
Published online: 30 July 2018

References

1. Tearney, G. J. et al. Scanning single-mode fiber optic catheter-endoscope for optical coherence tomography: erratum. *Opt. Lett.* **21**, 912 (1996).
2. Tearney, G. J. et al. In vivo endoscopic optical biopsy with optical coherence tomography. *Science* **276**, 2037–2039 (1997).
3. Fujimoto, J. G. et al. High resolution in vivo intra-arterial imaging with optical coherence tomography. *Heart* **82**, 128–133 (1999).
4. Yabushita, H. et al. Characterization of human atherosclerosis by optical coherence tomography. *Circulation* **106**, 1640–1645 (2002).
5. Kume, T. et al. Assessment of coronary arterial thrombus by optical coherence tomography. *Am. J. Cardiol.* **97**, 1713–1717 (2006).
6. Rollins, A. M. et al. Real-time in vivo imaging of human gastrointestinal ultrastructure by use of endoscopic optical coherence tomography with a novel efficient interferometer design. *Opt. Lett.* **24**, 1358–1360 (1999).
7. Li, X. D. et al. Optical coherence tomography: advanced technology for the endoscopic imaging of Barrett's esophagus. *Endoscopy* **32**, 921–930 (2000).
8. Sergeev, A. et al. In vivo endoscopic OCT imaging of precancer and cancer states of human mucosa. *Opt. Express* **1**, 432–440 (1997).
9. Lam, S. et al. In vivo optical coherence tomography imaging of preinvasive bronchial lesions. *Clin. Cancer Res.* **14**, 2006–2011 (2008).
10. Youngquist, R. C., Carr, S. & Davies, D. E. Optical coherence-domain reflectometry: a new optical evaluation technique. *Opt. Lett.* **12**, 158–160 (1987).
11. Huang, D. et al. Optical coherence tomography. *Science* **254**, 1178–1181 (1991).
12. Fujimoto, J. G. et al. Femtosecond optical ranging in biological systems. *Opt. Lett.* **11**, 150–152 (1986).
13. Fercher, A. F., Mengedoht, K. & Werner, W. Eye-length measurement by interferometry with partially coherent light. *Opt. Lett.* **13**, 186–188 (1988).
14. Choma, M., Sarunic, M., Yang, C. & Izatt, J. Sensitivity advantage of swept source and Fourier domain optical coherence tomography. *Opt. Express* **11**, 2183–2189 (2003).
15. de Boer, J. F. et al. Improved signal-to-noise ratio in spectral-domain compared with time-domain optical coherence tomography. *Opt. Lett.* **28**, 2067–2069 (2003).
16. Leitgeb, R., Hitzenberger, C. & Fercher, A. Performance of fourier domain vs. time domain optical coherence tomography. *Opt. Express* **11**, 889–894 (2003).
17. Wojtkowski, M., Bajraszewski, T., Targowski, P. & Kowalczyk, A. Real-time in vivo imaging by high-speed spectral optical coherence tomography. *Opt. Lett.* **28**, 1745–1747 (2003).
18. Yun, S., Tearney, G., de Boer, J., Iftimia, N. & Bouma, B. High-speed optical frequency-domain imaging. *Opt. Express* **11**, 2953–2963 (2003).
19. Liu, L. et al. Imaging the subcellular structure of human coronary atherosclerosis using micro-optical coherence tomography. *Nat. Med.* **17**, 1010–1014 (2011).
20. Spoler, F. et al. Simultaneous dual-band ultra-high resolution optical coherence tomography. *Opt. Express* **15**, 10832–10841 (2007).
21. Cimalla, P., Walther, J., Mehner, M., Cuevas, M. & Koch, E. Simultaneous dual-band optical coherence tomography in the spectral domain for high resolution in vivo imaging. *Opt. Express* **17**, 19486–19500 (2009).
22. Shu, X., Beckmann, L. & Zhang, H. Visible-light optical coherence tomography: a review. *J. Biomed. Opt.* **22**, 121707 (2017).
23. Kim, J. et al. Endoscopic micro-optical coherence tomography with extended depth of focus using a binary phase spatial filter. *Opt. Lett.* **42**, 379–382 (2017).
24. Xi, J. et al. Diffractive catheter for ultrahigh-resolution spectral-domain volumetric OCT imaging. *Opt. Lett.* **39**, 2016–2019 (2014).
25. Cui, D. et al. Flexible, high-resolution micro-optical coherence tomography endobronchial probe toward in vivo imaging of cilia. *Opt. Lett.* **42**, 867–870 (2017).
26. Drexler, W. et al. In vivo ultrahigh-resolution optical coherence tomography. *Opt. Lett.* **24**, 1221–1223 (1999).
27. Standish, B. A. et al. In vivo endoscopic multi-beam optical coherence tomography. *Phys. Med. Biol.* **55**, 615–622 (2010).
28. Singh, K., Yamada, D. & Tearney, G. Astigmatism corrected common path probe for optical coherence tomography. *Lasers Surg. Med.* **49**, 312–318 (2017).
29. Fang, Q. et al. Ultrahigh-resolution optical coherence elastography through a micro-endoscope: towards in vivo imaging of cellular-scale mechanics. *Biomed. Opt. Express* **8**, 5127–5138 (2017).
30. Shishkov, M., Bouma, B. E. & Tearney, G. J. System and method for optical coherence imaging. US patent 20060067620A1 (2006).
31. Ohmi, S. et al. Gradient-index rod lens made by a double ion-exchange process. *Appl. Opt.* **27**, 496–499 (1988).
32. Khorasaninejad, M. & Capasso, F. Metalenses: versatile multifunctional photonic components. *Science* **358**, eaam8100 (2017).
33. Yu, N. et al. Light propagation with phase discontinuities: generalized laws of reflection and refraction. *Science* **334**, 333–337 (2011).
34. Khorasaninejad, M. et al. Metalenses at visible wavelengths: diffraction-limited focusing and subwavelength resolution imaging. *Science* **352**, 1190–1194 (2016).
35. Huang, Y. W. et al. Aluminum plasmonic multicolor meta-hologram. *Nano Lett.* **15**, 3122–3127 (2015).
36. Balthasar Mueller, J. P., Rubin, N. A., Devlin, R. C., Groever, B. & Capasso, F. Metasurface polarization optics: independent phase control of arbitrary orthogonal states of polarization. *Phys. Rev. Lett.* **118**, 113901 (2017).
37. Ralston, T. S., Marks, D. L., Carney, P. S. & Boppart, S. A. Interferometric synthetic aperture microscopy. *Nat. Phys.* **3**, 129–134 (2007).
38. Khorasaninejad, M. & Crozier, K. B. Silicon nanofin grating as a miniature chirality-distinguishing beam-splitter. *Nat. Commun.* **5**, 5386 (2014).
39. Khorasaninejad, M. & Capasso, F. Broadband multifunctional efficient meta-gratings based on dielectric waveguide phase shifters. *Nano Lett.* **15**, 6709–6715 (2015).
40. Fercher, A. F., Hitzenberger, C. K., Kamp, G. & El-Zaiat, S. Y. Measurement of intraocular distances by backscattering spectral interferometry. *Opt. Commun.* **117**, 43–48 (1995).
41. Ha Usler, G. & Lindner, M. W. "Coherence radar" and "spectral radar"-new tools for dermatological diagnosis. *J. Biomed. Opt.* **3**, 21–31 (1998).
42. Khorasaninejad, M., Chen, W. T., Oh, J. & Capasso, F. Super-dispersive off-axis meta-lenses for compact high resolution spectroscopy. *Nano Lett.* **16**, 3732–3737 (2016).
43. Khorasaninejad, M. et al. Achromatic metasurface lens at telecommunication wavelengths. *Nano Lett.* **15**, 5358–5362 (2015).
44. Khorasaninejad, M. et al. Achromatic metalens over 60 nm bandwidth in the visible and metalens with reverse chromatic dispersion. *Nano Lett.* **17**, 1819–1824 (2017).
45. Yun, S. H. et al. Comprehensive volumetric optical microscopy in vivo. *Nat. Med.* **12**, 1429–1433 (2006).
46. Yun, S., Tearney, G., de Boer, J. & Bouma, B. Removing the depth-degeneracy in optical frequency domain imaging with frequency shifting. *Opt. Express* **12**, 4822–4828 (2004).
47. Hariri, L. P. et al. Toward the guidance of transbronchial biopsy: identifying pulmonary nodules with optical coherence tomography. *Chest* **144**, 1261–1268 (2013).
48. Hariri, L. P. et al. Seeing beyond the bronchoscope to increase the diagnostic yield of bronchoscopic biopsy. *Am. J. Respir. Crit. Care Med.* **187**, 125–129 (2013).
49. Adams, D. C. et al. Birefringence microscopy platform for assessing airway smooth muscle structure and function in vivo. *Sci. Transl. Med.* **8**, 359ra131 (2016).
50. Hariri, L. P. et al. Endobronchial optical coherence tomography for low-risk microscopic assessment and diagnosis of idiopathic pulmonary fibrosis in vivo. *Am. J. Respir. Crit. Care Med.* **197**, 949–952 (2018).
51. Nadkarni, S. K. et al. Measurement of collagen and smooth muscle cell content in atherosclerotic plaques using polarization-sensitive optical coherence tomography. *J. Am. Coll. Cardiol.* **49**, 1474–1481 (2007).

Acknowledgements

This project was supported by funding from the National Institutes of Health (R01CA167827, R01HL133664 awarded to M.J.S.), Air Force Office of Scientific Research (MURI: FA9550-14-1-0389, FA9550-16-1-0156 awarded to F.C.), and the LUNGevity Foundation/Upstage Lung Cancer. Y.-W.H. and C.-W.Q. are supported by the National Research Foundation, Prime Minister's Office, Singapore under its Competitive Research Program (CRP award no. NRF-CRP15-2015-03). This work was performed in part at Harvard's Center for Nanoscale Systems (CNS), a member of the National Nanotechnology Coordinated Infrastructure (NNCI), supported by the National Science Foundation (NSF) under NSF award no. 1541959. Y.-W.H. thanks Y.-C. Chen for helpful comments and discussions.

Author contributions

H.P., M.K. and Y.-W.H. carried out analyses, fabricated endoscopes, and planned and executed the experiments. Z.S. performed computational analysis for metalens design. L.P.H., M.J.S. and H.P. performed the ex vivo and in vivo imaging. M.J.S. and D.C.A. implemented the OCT system. H.P. and D.C.A. processed imaging data. V.D. and A.Z. assisted with experiments and fabrication. H.P. prepared the original manuscript with significant contributions from M.K., Y.-W.H. and C.-W.Q. M.J.S. and F.C. supervised the project and participated in manuscript preparation.

Competing interests

H.P., M.K., Y.-W.H., Z.S., M.J.S. and F.C. are the inventors on a relevant provisional patent application (application number: 62598455) owned by Harvard University and Massachusetts General Hospital.

Additional information

Supplementary information is available for this paper at https://doi.org/10.1038/s41566-018-0224-2.

Reprints and permissions information is available at www.nature.com/reprints.

Correspondence and requests for materials should be addressed to F.C. or M.J.S.

Publisher's note: Springer Nature remains neutral with regard to jurisdictional claims in published maps and institutional affiliations.

Methods

Fabrication process. The metalenses were fabricated using lithographic techniques[38,39]. A 750-nm-thick a-Si layer was deposited on a 170-μm-thick glass substrate using plasma-enhanced chemical vapour deposition. The sample was spin-coated with a double layer of positive electron-beam resist (MicroChem, PMMA495K A4 and PMMA950K A2) and an additional layer of conductive polymer (Showa Denko, ESPACER 300) to avoid charging effects during electron-beam lithography (EBL). Nanopillar mask patterns were defined using EBL (Elionix, ELS-F125) followed by developing in a 1:3 mixture of methyl isobutyl ketone (MIBK) and isopropyl alcohol (IPA) and then deposition of a 30-nm-thick aluminum layer by thermal evaporation and lift-off. Inductively coupled plasma-reactive ion etching was used to etch the nanopillar structures. Anisotropic etching was achieved using a mixture of SF_6 and C_4F_8. The aluminium mask was eventually removed by immersing the sample in the developer (Shipley, MF319). The overall size of the fabricated metalens was approximately 290 μm × 290 μm.

The fabrication of the resolution target included spin-coating of a 500-μm-thick quartz substrate with a positive electron-beam resist layer (Zeon Chemicals, ZEP520A) and a conductive polymer layer (Showa Denko, ESPACER 300) and defining the pattern using EBL, followed by deposition of a 50-nm-thick gold layer by thermal evaporation and lift-off.

OCT imaging and data processing. For comparison with the nano-optic endoscope, a commercial GRIN lens catheter (Dragonfly OPTIS Imaging Catheter) from St Jude Medical and a ball lens catheter fabricated in Massachusetts General Hospital were used. The Partners Human Research Committee Institutional Review Board (IRB) approved ex vivo imaging of human lung specimens (protocol 2010-P-002214/1) and the Institutional Animal Care and Use Committee (IACUC) at Massachusetts General Hospital approved the in vivo endobronchial OCT of the sheep (protocol 2014N000048). Structural OCT images were generated by standard processing techniques as previously described[46]. Processing included fast Fourier transform of the background-subtracted raw data, re-centring and zeroing the negative portion of the data to remove depth degeneracy, and compensating dispersion and linearizing *k*-space mathematically. The square root of squares of signals from two polarization channels in logarithmic scale represents OCT structural images.

Data availability. The data that support the plots within this paper and other findings of this study are available from the corresponding authors upon reasonable request.